RESEARCH ARTICLE
SPACE PHYSICS: MAGNETOSPHERIC PHYSICS

Earth and Planetary Physics
8: 59–69, 2024
doi: 10.26464/epp2023059

Deformations at Earth's dayside magnetopause during quasi-radial IMF conditions: Global kinetic simulations and Soft X-ray Imaging

ZhongWei Yang[1], RiKu Jarvinen[2], XiaoCheng Guo[1*], TianRan Sun[1*], Dimitra Koutroumpa[3], George K. Parks[4], Can Huang[5], BinBin Tang[1], QuanMing Lu[6], and Chi Wang[1]

[1]State Key Laboratory of Space Weather, National Space Science Center, Chinese Academy of Sciences, Beijing 100190, China;

[2]Finnish Meteorological Institute, FI-00101 Helsinki, Finland;

[3]LATMOS/IPSL, CNRS, UVSQ Université Paris-Saclay, Sorbonne Université, Guyancourt, 78280, France;

[4]Space Sciences Laboratory, University of California, Berkeley, California 94720, USA;

[5]CAS Engineering Laboratory for Deep Resources Equipment and Technology, Institute of Geology and Geophysics, Chinese Academy of Sciences, Beijing 100029 China;

[6]Deep Space Exploration Laboratory/School of Earth and Space Sciences, University of Science and Technology of China, Hefei 230026, China

Key Points:

- We produce soft X-ray images of the dayside magnetopause with a 3-D global hybrid simulation under a quasi-radial interplanetary magnetic field condition.
- Magnetopause deformations are highly coherent with the magnetosheath high speed jets generated at the quasi-parallel region of the bow shock.
- High-speed jet structures within the magnetosheath can generate soft X-ray signatures in line-of-sight integrated images.

Citation: Yang, Z. W., Jarvinen, R., Guo, X. C., Sun, T. R., Koutroumpa. D., Parks, G. K., Huang, C., Tang, B. B., Lu, Q. M., and Wang, C. (2024). Deformations at Earth's dayside magnetopause during quasi-radial IMF conditions: Global kinetic simulations and Soft X-ray Imaging. *Earth Planet. Phys.*, *8*(1), 59–69. http://doi.org/10.26464/epp2023059

Abstract: The Solar wind Magnetosphere Ionosphere Link Explorer (SMILE) is a joint mission of the European Space Agency (ESA) and the Chinese Academy of Sciences (CAS). Primary goals are investigating the dynamic response of the Earth's magnetosphere to the solar wind (SW) impact via simultaneous in situ magnetosheath plasma and magnetic field measurements, X-Ray images of the magnetosheath and magnetic cusps, and UV images of global auroral distributions. Magnetopause deformations associated with magnetosheath high speed jets (HSJs) under a quasi-parallel interplanetary magnetic field condition are studied using a three-dimensional (3-D) global hybrid simulation. Soft X-ray intensity calculated based on both physical quantities of solar wind proton and oxygen ions is compared. We obtain key findings concerning deformations at the magnetopause: (1) Magnetopause deformations are highly coherent with the magnetosheath HSJs generated at the quasi-parallel region of the bow shock, (2) X-ray intensities estimated using solar wind H^+ and self-consistent O^{7+} ions are consistent with each other, (3) Visual spacecraft are employed to check the discrimination ability for capturing magnetopause deformations on Lunar and polar orbits, respectively. The SMILE spacecraft on the polar orbit could be expected to provide opportunities for capturing the global geometry of the magnetopause in the equatorial plane. A striking point is that SMILE has the potential to capture small-scale magnetopause deformations and magnetosheath transients, such as HSJs, at medium altitudes on its orbit. Simulation results also demonstrate that a lunar based imager (e.g., Lunar Environment heliospheric X-ray Imager, LEXI) is expected to observe a localized brightening of the magnetosheath during HSJ events in the meridian plane. These preliminary results might contribute to the pre-studies for the SMILE and LEXI missions by providing qualitative and quantitative soft X-ray estimates of dayside kinetic processes.

Keywords: collisionless shock; SMILE mission; foreshock

1. Introduction

In-situ spacecraft observations in the near-Earth plasma environment (e.g., MMS, Cluster, Van Allen Probes, THEMIS, Geotail, Double Star) have made important contributions in revealing dynamic and kinetic problems of the solar wind interaction with the Earth's magnetosphere. These observations provide excellent opportunities for understanding the microphysics of collisionless shocks, magnetic reconnection, and wave-particle interactions, as well as cross-scale energy release and dissipation by substorms and turbulence. On the other hand, remote observations of radio emissions, optical light, infrared, extreme ultraviolet (EUV), X-ray,

First author: Z. W. Yang, zwyang@swl.ac.cn
Correspondence to: X. C. Guo, xcguo@spaceweather.ac.cn
T. R. SUN, trsun@spaceweather.ac.cn
Received 29 APR 2023; Accepted 10 JUL 2023.
First Published online 08 AUG 2023.

gamma-ray, and energetic neutral atoms are widely used for remote objects. These imaging techniques provide a new way for visualizing global pictures of the Earth's exosphere, plasmasphere, inner magnetosphere, magnetosheath, magnetotail, and the cusp region (e.g., TWINS, IBEX, XMM-Newton), as well as in solar activities and heliospheric structures (e.g., Parker Solar Probe, Solar Orbiter).

Early ROSAT observations of X-ray and EUV emission from comet C/Hyakutake have been reported by Lisse et al. (1996). Some mechanisms, such as thermal bremsstrahlung associated with hot electrons, possibly due to solar wind interaction effects, are suggested to explain the mechanism of this emission. Cravens (1997) proposed that the solar wind contains a large number of heavy ion species with a range of charge states (e.g., C^{6+}, O^{7+}, O^{8+}). These ions will readily charge transfer with cometary or planet's exospheric neutrals, producing ions that can be highly excited and consequently emit photons in the X-ray and EUV part of the spectrum. This solar wind charge exchange mechanism is abbreviated as SWCX. Thereafter, an empirical formula that depends on the local neutral density, solar wind density, solar wind speed, and charge-exchange cross-section is proposed for the quantitative estimation of the X-ray intensity (Cravens 2000; Schwadron and Cravens 2000). Cravens et al. (2001) found that a significant positive correlation exists between the solar wind fluxes and the soft X-ray intensity. Furthermore, XMM-Newton observations indicate that the elevated high-valence ion abundance inside a coronal mass ejection (CME), particularly for Ne^{9+}, Mg^{11+}, Mg^{12+}, etc., favors the enhancement of Earth's magnetospheric soft X-ray emissions (Zhang YJ et al. 2022).

SWCX emissions are commonly observed in the heliosphere at comets (Lisse et al. 1996; Wegmann and Dennerl 2005), Earth (Wargelin et al. 2004; Fujimoto et al. 2007), the Moon (Collier et al. 2014), Jupiter (Branduardi-Raymont et al. 2004), and Mars (Dennerl et al. 2006). Sibeck et al. (2018) reviewed observations of soft X-ray emissions have become a powerful tool for panoramic imaging of the planetary magnetosphere and plasma environment. Currently, new and future space missions, specifically designed for X-ray imaging of the vast planetary space weather system, including the ESA/JAXA BepiColombo mission, SMILE ESA–CAS joint mission, NASA STORM missions, CubeSat/small spacecraft missions (e.g., NASA CuPID, JAXA GEO-X), and future lunar-based missions (e.g., NASA LEXI, Chinese Chang'e/SXI), were proposed and successively implemented for studying "charge-exchange," a poorly understood phenomenon that occurs when the solar wind collides with planetary exosphere and neutral gas in the heliosphere.

To support the development of new X-ray missions, numerical simulations are crucial for pre-studies. Several numerical models have been developed to simulate soft X-ray imaging and determine detectability. Empirical models (Holmström et al. 2001) have been used to explore X-ray imaging of the solar wind-Mars interaction. Hybrid simulations and test particle calculations have been used to compute contributions from SWCX processes to X-ray emissions from Venus (Gunell et al. 2007) and Mars (Koutroumpa et al. 2012). MHD simulations are commonly used to accurately describe the shape of global structures of the terrestrial magnetosphere during its interaction with the solar wind. By combining an empirical exosphere neutral profile with the solar wind flux from MHD simulations, the soft X-ray emission can be estimated using Cravens' formula. Studies have discussed the soft X-ray visibility of the solar storm compressed magnetopause, the cusp region, flank Kelvin–Helmholtz (K-H) waves, and magnetic reconnection associated outflows and flux transfer events (FTEs) in detail (e.g., Sun TR et al. 2015, 2019; Jorgensen et al. 2019; Matsumoto and Miyoshi 2022).

Previous models and simulations have made a lot of achievements in the study of Earth's X-ray emissions. However, it is still an open question whether the soft X-ray excited by moderate-scale dynamic structures in the magnetosheath and magnetosphere is visible. Many cross-scale instantaneous structures have been observed from the foreshock all the way to the magnetopause. Here, we list some structures highly associated with at least ion kinetic behaviors: (1) The foreshock region is filled with ULF waves, shocklets, SLAMS, and other nonlinear structures, and even magnetic reconnections. Schwartz and Burgess (1991) made a patchwork for the foreshock. The foreshock waves and structures have been clearly evidenced in both kinetic simulations (e.g., Blanco–Cano et al. 2006; Palmroth et al. 2015; Otsuka et al. 2019; Chen LJ et al. 2021), and observations (Wilson et al. 2013; Jiang K et al. 2021; Wang S et al. 2021; Huang SY et al. 2022; Liu MZ et al. 2022). (2) Both kinetic simulations and MMS observations reveal that the bow shock not only undergoes back and forth swings under the turbulent solar wind, but also can experience kinetic-scale ripples (Burgess et al. 2005; Johlander et al. 2016) and self-reforming cycles (Lembège et al. 2004; Yang ZW et al. 2020; Liu TZ et al. 2021). (3) Magnetosheath high speed jets (HSJs) refer to an enhancement in the anti-sunward bulk velocity and dynamic pressure based on the x component of the ion velocity (Hietala and Plaschke 2013; Plaschke et al. 2018). A recent study proposes that a fraction of HSJs is a direct consequence of shock reformation (Rapitis et al. 2022), and they may be related to "throat aurora" and corresponding magnetopause distortion (Han DS et al. 2017). 2-D hybrid simulations have been employed to study the HSJ property, size, lifetime, and associated jet-driven bow wave (e.g., Karimabadi et al. 2014; Hao YF et al. 2017; Preisser et al. 2020; Palmroth et al. 2021; Guo J et al. 2022; Tinoco-Arenas et al. 2022). They find that the jets are associated with the porous quasi-parallel shock front, and the scale size of jets can reach about 2.5–5 R_E. (4) In addition, magnetopause asymmetric reconnection (Burch et al. 2016), magnetosheath reconnections at both electron and ion scales (Phan et al. 2018; Lu QM et al. 2021; Bessho et al. 2022), small-scale current filaments (Gingell et al. 2020), magnetopause K-H waves (Guo ZF et al. 2010; Li WY et al. 2012), and associated vortex-induced reconnections (Nakamura et al. 2017) also play important roles in the cross-scale process and energy conversion during the Earth–solar wind interaction.

Some potential soft X-ray imaging objects, such as solar storms, K-H waves, and FTE events, have been investigated based on global MHD simulations (e.g., Sun TR et al. 2015, 2019; Jorgensen et al. 2019; Matsumoto and Miyoshi 2022). In this study, we focus on HSJs, which are typically observed downstream from the quasi-parallel bow shock, and are highly associated with ion dynamic and kinetic processes in 3-D. Cluster and MMS simultaneous observations provide insight into HSJs. Escoubet et al. (2020) found that HSJs are not localized into small regions but could

span a region larger than 10 R_E, especially when the quasi-parallel shock covers the entire dayside magnetosphere under radial interplanetary magnetic field (IMF). The magnetopause can have multiple independent indentation places under the continuous impacts of HSJs. The magnetopause is deformed and can move in opposite directions at different places. It cannot, therefore, be considered as a smooth surface anymore but rather as a surface full of local indents. One striking point is that a large number of observations indicate that long radial IMF events can last from about 3–10 hours (Farrugia et al. 2014; Pi et al. 2022) to 1–2 days (Watari et al. 2005). Under such long-duration IMF solar wind conditions, the foreshock has enough time to grow and reach a mature state. In this case, the magnetopause around the sunset point may suffer continuous disturbances of HSJs. If so, what the soft X-ray imaging will look like remains to be further simulated and analyzed.

In this paper, we focus on the dynamics of the foreshock and magnetosheath to address three primary questions: (1) How do HSJs continuously affect the magnetopause under radial IMF events? (2) What is the global picture and fate of these jets and their resulting magnetopause indents at different locations in 3D? (3) What is the timescale of the magnetopause response to HSJs, and (4) can it be identified in soft X-ray intensity images by SMILE, LEXI, and other lunar-based missions?

2. Simulation Model

In this paper, the interaction of the solar wind with Earth's magnetosphere has been simulated by the three-dimensional (3-D) global hybrid simulation platform RHybrid (e.g., Jarvinen et al. 2018, 2020, 2022; Kallio et al. 2022). The model setup includes the undisturbed, upstream solar wind ions injected in the simulation from the front (+x) wall along the −x direction with a drifting Maxwellian velocity distribution. Within the simulation domain, ion velocity distributions evolve according to model calculation self-consistently coupled with the evolution of the magnetic field. The perpendicular components of the undisturbed IMF to the flow (B_y, B_z) convect in the simulation domain frozen-in to the solar wind plasma, whereas the radial, flow-aligned component (B_x) is implemented as a constant magnetic field profile. Earth's magnetic field is estimated as a 3-D dipole field (Fatemi et al. 2018; Jarvinen et al. 2020; Omelchenko et al. 2021) instead of a mirror dipole (Raeder 2003; Hu YQ et al. 2007; Lin Y et al. 2014). Magnetospheric solar wind interaction, including different regions such as the dayside and nightside magnetosphere, magnetosheath and the foreshock and the boundaries like the bow shock and the magnetopause, forms self-consistently when the magnetized solar wind plasma flow encounters the geomagnetic field and the planetary environment. Electrons are modeled as a charge-neutralizing adiabatic fluid. The inner boundary is assumed at the geocenter distance of r = 3 R_E. It is implemented as a perfect conducting sphere on which precipitated particles are absorbed.

Usually, the simulated Earth radius R_E is typically reduced to an order of 10 d_{i0} (the upstream solar wind ion inertial length) in order to ensure the appearance of an Earth-like magnetosphere (e.g., Blanco-Cano et al. 2006; Lin Y et al. 2014) and to save considerable computational costs in global hybrid simulations. In this paper, the value of R_E = 1200 km. A set of solar wind parameters (e.g., Lepri et al. 2013; Schwadron and Cravens 2000; Larrodera and Cid 2020) are used to mimic the space environment for the SMILE mission, which is scheduled to launch in 2025 during solar maximum. The solar wind ions consist of protons with a bulk velocity of 450 km/s and a number density of 7 cm^{-3}, and highly ionized minor species O^{7+}. The IMF magnitude is 10 nT, corresponding to a solar wind ion gyro-frequency of $\Omega_0 = 0.958 \approx 1\ s^{-1}$. The magnetic Reynolds number is set to 1.2×10^7. Uniform grid cells with a size of $\Delta x = \Delta y = \Delta z = 0.08\ R_E$ are used throughout the box. The cell dimensions are chosen as $n_x \times n_y \times n_z = 500 \times 600 \times 600$. A total of about ten billion particles are used. A typical time step is $\Delta t = 0.01$ s. More details of parameter setups are summarized in Table 1.

Table 1. Global hybrid model setups and solar wind conditions.

Parameters	Value
Number of grid cells ($n_x \times n_y \times n_z$)	$500 \times 600 \times 600$
Grid cell size (Δx)	$(100\ km)^3 = (R_E/12)^3$
Time step (Δt)	10 ms
SW bulk velocity vector [V_x, V_y, V_z]	[−450, 0, 0] km/s
SW H^+ density	7 cm^{-3}
SW O^{7+} density	10^{-4} cm^{-3}
SW H^+ temperature	15×10^4 K
SW O^{7+} temperature	15×10^4 K
SW e^- temperature	15×10^4 K
IMF vector [B_x, B_y, B_z]	[−9.96, 0.6, 0.6] nT
IMF spiral angle	4° (away sector)
IMF magnitude	10 nT
Alfvén Mach number	5.46
Magnetosonic Mach number	4.79
Dipole strength B_0 at the equator on the surface	4.5 μT

3. Simulation Results

3.1 Quasi-parallel IMF Condition

Under radial solar wind conditions, there are at least two initiation methods for simulating the interaction between solar wind and planetary magnetospheres. The first involves introducing a dipole field within the IMF, allowing the dipole field strength to gradually diminish with increasing distance from the Earth's core, transitioning to a purely solar wind magnetic field (e.g., Fatemi et al. 2020; Chen LJ et al. 2021). The second method employs a mirrored dipole field approach on the sunward side, such as placing a mirrored dipole at x = +30 Earth radii, superimposing its magnetic field with the original field, and ultimately replacing the magnetic field in the upstream region at x = +15 Earth radii with a purely solar wind magnetic field (e.g., Hu YQ et al. 2007; Lin Y et al. 2014). Both of the initial configurations yield satisfactory magnetospheric morphologies and are extensively utilized in astrophysical and

space physics simulations for Hermean-type planetary magnetospheres. Without loss of generality, this study adopts the first method for initiating the simulation.

Figure 1 illustrates the interaction between the solar wind and the Earth's magnetosphere under radial IMF conditions, as well as the formation process of the bow shock. Panels from left to right represent snapshots of the number density of H^+ ions at different times t = 3 s, 70 s, 220 s, and 235 s, respectively. Figure 1a shows the Earth's dipole field at the beginning of the simulation. The magnetosphere begins to expand and gradually form. At later time (Figure 1b), the Earth's magnetosphere including key structures (e.g., the magnetopause, the magnetosheath, cusp regions, and the bow shock), has been initially formed. A fraction of the incident solar wind ions are reflected at the bow shock front. These back-streaming ions interact with the freshly incident solar wind, causing low-frequency waves in the foreshock region. In Figure 1c–d, the foreshock has reached a mature form under the long-term radial solar wind conditions.

Yellow arrows in Figure 1c–d indicate that the foreshock low-frequency wave structure can undergo nonlinear evolution and become steep when approaching the Earth's bow shock. These nonlinear structures have been widely observed at quasi-parallel shocks (Burgess et al. 1989; Burgess and Scholer 2013). Previous local simulations clearly revealed that such steepening foreshock transients are associated with magnetosheath dynamic structures, such as HSJs (e.g., Hao Y et al. 2016; Guo J et al. 2022; Tinoco-Arenas et al. 2022). Both of spacecraft observations (e.g., Hietala et al. 2009; Plaschke et al. 2018; Escoubet et al. 2020; Rapitis et al. 2022) and global simulations (e.g., Chen LJ et al. 2021; Ng et al. 2021; Palmroth et al. 2021; Guo J et al. 2022) clearly evidenced that HSJs generated in the immediate downstream of quasi-parallel shock can lead to magnetopause indents.

In the next section, we will take HSJs as an example to study magnetopause deformations (including indentation and protrusion).

3.2 Magnetopause Deformation

Figure 2a (at t = 235 s) shows that the magnetopause is being compressed inward by the magnetosheath transients, forming a concave shape as indicated by the white arrow in the enlarged view (Figure 1d). A standard streamline method (LIC) is adopted to display the magnetic field lines of the forced magnetosphere. The magnetic field lines in the concave magnetopause region are locally bent inward, rather than moving as a whole. This is a crucial and can be different from the mechanism of magnetopause indents compressed by CME-driven shocks in a large-scale. Figure 2b and c are snapshots of the magnetopause at non-concave and concave times (t = 160 s and 235 s), respectively. Figure 2c depict an zoom-in view of the region where the magnetopause is affected HSJs. From Figure 2c, it can be clearly seen that there is a strong HSJ in the dayside direction of the concave region of the magnetopause. In comparison, the magnetopause without the HSJ impact (Figure 2b, t = 160 s) is relatively quiet and no obvious deformation as that at t = 235 s. It is interesting to note that there is a HSJ located near z = −6 R_E, where the magnetopause is slightly concave due to the influence of the HSJ. However, this HSJ is off the dayside and exists in the magnetosheath region at a relative high latitude. The plasma flow in the local magnetosheath has begun to deflect, so the HSJ does not form a strong hit on the magnetopause like it did at the dayside. In summary, the foreshock continuously generates dynamic magnetosheath transients such as HSJs, which can cause deformation of the magnetopause. Tinoco-Arenas et al. (2022) used local simulations to statistically analyze the evolution of various transient structures such as HSJ, transient flux enhancements, and high speed plasmoids downstream of quasi-parallel shocks. The formation mechanism will not

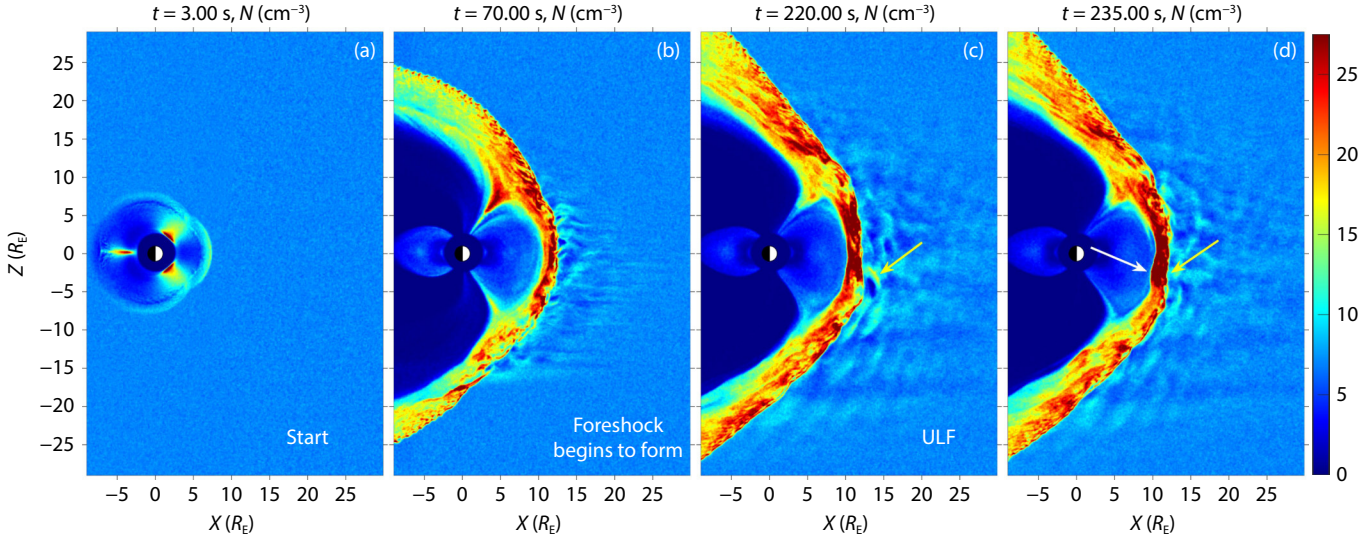

Figure 1. The magnetosphere forms by interaction between the solar wind and the geomagnetic field under quasi-radial IMF condition. Slices of the total ion density n_{tot} in the meridian plane at t = 3, 70, 220 and 235 s are shown in panels (a–d). (a–b) The magnetosphere and foreshock begin to form. (c) A fraction of foreshock ULF waves undergo nonlinear evolution and become steepening before reaching the bow shock front (marked by a yellow arrow). (c–d) Magnetopause indents (denoted by a white arrow) caused by the magnetosheath HSJs downstream of the mature quasi-parallel shock.

be further elaborated here, and this paper only focuses on the magnetopause deformation caused by such transient structures in response to soft X-ray imaging. Nevertheless, it is still worth mentioning that, unlike the planar shock in hybrid and PIC simulations (e.g., Winske and Quest, 1988; Burgess et al., 1989; Lembège and Savoini, 1992; Scholer et al., 2003; Matsukiyo and Scholer, 2003; Yang ZW et al., 2020), global simulations indicate that the solar wind is deflected around the Earth's magnetosphere in the magnetosheath. The transients are more likely impact the magnetopause about the subsolar point.

Figures 3a–c represent the time-evolution of ion number densities $\log_{10}N$ sampled at different locations: A, B and C (denoted in Figure 2). To understand characteristics of the magnetopause depressions, Figures 3d–f show the time series of *x*-directional dynamic pressure P_{dx}, temperature *T*, and X-ray intensity *P* corresponding to the sampling location C. This dynamic evolution process cannot be reflected by shock and magnetopause empirical models. High-resolution data from Magnetospheric MultiScale (MMS) have been continuously released, and the kinetic processes of shock front rippling and self-reformation have been successively confirmed. These mechanisms may result in variations to the location and configuration of the bow shock, and most of the changes

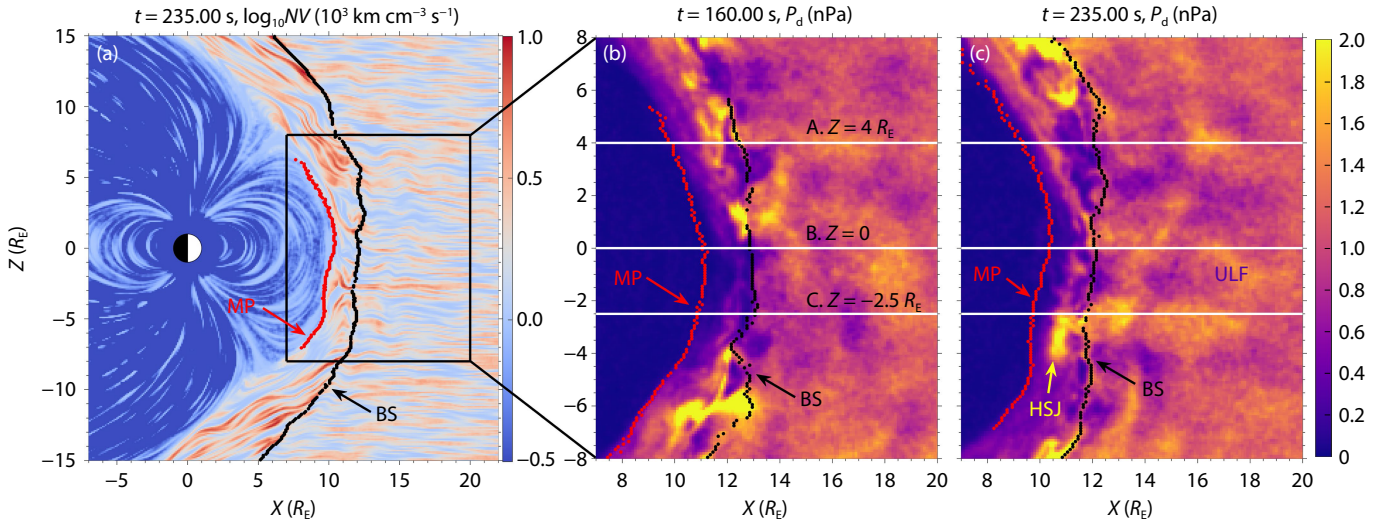

Figure 2. (a) The dayside deformed magnetopause at *t* = 235 s. Magnetic field lines are visualized using the linear integral convolution (LIC) method (Karimabadi et al., 2014) over the ion flux *NV*. The black dotted curve represents the plasma density at the bow shock (BS) that is 2 times (basically the same if we choose 1.5–2.5) the background solar wind ion density in the upstream undisturbed region. The magnetopause (MP, red dotted curve) can be approximately derived by tracing ions trapped by closed magnetic field lines of the magnetosphere. (b–c) Zoom-in views of the region within the black rectangle in (a). Snapshots of solar wind dynamic pressure profiles P_{dx} at *t* = 160 s and 235 s are plotted, respectively.

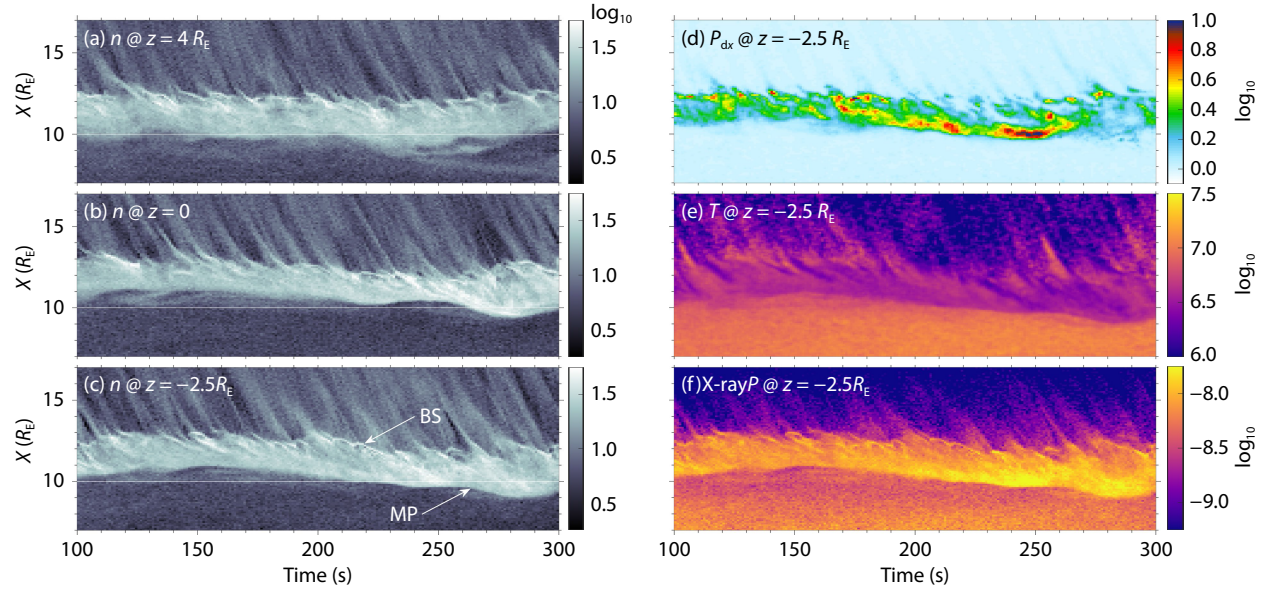

Figure 3. (a–c) Stack-plots of the bow shock and magnetopause positions versus time in a set of sampling boxes denoted by A, B, and C in Figure 2b–c. For the sampling place C, panels (d–f) show the corresponding time-evolution of P_{dx}, ion temperature *T* in log scale, and X-ray intensity *P* at the sampling place C.

are concentrated on the ion scale. Rapitis et al. (2022) show in situ evidence of HSJs generated at the Earth's bow shock as a direct consequence of shock self-reformation. In this paper, from a global simulation perspective, we trace the evolution of various regions from the foreshock to the magnetopause at a relatively large scale (in an order of ~R_E). Figure 3d shows that magnetopause depressions are usually accompanied by an increase in the dynamic pressure P_{dx} in the magnetosheath. Under the impact of the HSJs, the ion temperature inside the magnetopause does not significantly change (Figure 3e). In Figure 3f, one striking point is that the dynamic pressure can locally enhance the X-ray intensity within the magnetosheath ahead of the magnetopause. Furthermore, Figures 3b–c show that the magnetopause at $Z = 0$ and $Z = -2.5$ R_E exhibited earthward indentation at about t = 270 s. This is mainly due to the dragging of magnetic field lines caused by the HSJ impacting the magnetopause near the subsolar point.

In summary, magnetopause depressions caused by magnetosheath transients could last 20–50 seconds. This will be more advantageous for the X-ray imaging. Of course, the quality of imaging also depends on many factors, such as the counts of X-ray photons, the field of view (FOV) at a certain orbit, the spatial and temporal resolutions, the exposure time, and the background noise. The estimation of X-ray imaging considering all factors mentioned above is beyond the scope of this paper and depend on the final parameters of the SMILE/SXI. The motivation of this work is to suggest more potential kinetic processes and structural objects that could be observed by soft X-ray instruments in the future. The soft X-ray calculated from the sampling area (Figure 3f) suggests that magnetopause deformations imaged by soft X-rays instrument can be possible. In the next subsection, we will further study the three-dimensional soft X-ray imaging of magnetosheath transients and magnetopause indents from perspectives of local intensities and line-of-sight (LOS) integrations.

3.3 Soft-X Ray Imaging

In this study, the X-ray intensity of the geocoronal SWCX emission for a particular line-of-sight (LOS) I can be estimated by the line integration of volume emission rate (P) as in previous investigations (e.g., Cravens 2000; Sun TR et al. 2019; Connor et al. 2021).

$$I = \frac{1}{4\pi}\int P_{dr} = \frac{1}{4\pi}\int \alpha n_H n_{sw} V_{eff} dr, \tag{1}$$

where n_H and n_{sw} are number densities of exospheric hydrogen and solar wind proton, respectively. The effective collision speed is estimated by the solar wind velocity V_{sw} and thermal speed V_{th} as $V_{eff} = \sqrt{V_{sw}^2 + V_{th}^2}$ in Equation (1). This equation expresses I in keV cm^{-2} s^{-1} sr^{-1}. It is important to note that protons do not produce soft X-rays. Instead, heavy solar wind ions such as C^{5+}, C^{6+}, Ne^{9+}, O^{7+}, O^{8+}, Mg^{11+}, Mg^{12+} emit soft X-rays through the SWCX (e.g., Cravens 2000; Sibeck et al. 2018; Zhang et al. 2022). For instance, the interaction $O^{7+} + H \rightarrow O^{6+*} + H^+$ in which an electron is transferred from an exospheric hydrogen to an solar wind oxygen ion, leaves the oxygen ion an excited state. The ion then emits a photon when it decays to a lower energy state and thus may lead to the satellite detection of soft X-rays. The heavy ions in the solar wind have a very small proportion and are reasonably considered to be test particles in previous MHD and hybrid simulations. Typically, the X-ray intensity emitted by heavy ions is estimated by combing the proton parameters and an interaction efficiency factor. In this paper, our simulation are performed in the presence of self-consistent solar wind H^+ and O^{7+} ions, which allows us to independently estimate X-ray intensities based on O^{7+} or H^+ ions, respectively. By applying the interaction efficiency factor (α), the proton-based value in Equation (1) is converted into the soft X-ray emissivity generated by the source ions. Cravens (2000) gave a rough estimate of α encompassing all the detailed atomic physics. Based on summarized parameter lists (e.g., Schwadron and Cravens 2000; Cravens et al. 2001; Pepino et al. 2004; Koutroumpa et al. 2006; Sibeck et al. 2018), we use an interaction efficiency factor value of $\alpha = 10^{-15}$ (eV cm^2) under a solar wind speed about 450 (km/s), following previous simulations (e.g., Sun TR et al. 2019; Grandin et al. 2024) and reference therein. Although this setup is widely used, it is worthy to note that the value of α is quite uncertain and depends on solar wind conditions (Robertson and Cravens 2003). An analytical model from Cravens et al. (2001) for the neutral density, given as

$$n_H = 25 \times (10R_E/r)^3, \tag{2}$$

where r is the distance of the considered location to the Earth's center. The unit of 25 is cm^{-3}. The X-ray intensity P of heavy ions, e.g., O^{7+} also can be estimated, following Schwadron and Cravens (2000) and reference therein.

$$P = \sigma_{sw}[O^{7+}/O][O/H]F_{sw}n_H, \tag{3}$$

where σ_{sw} is the charge-exchange cross section that depends on the solar wind species and charge state. This equation expresses P in keV cm^{-3} s^{-1}. Parameters $\sigma_{sw} = 12 \times 10^{-15}$ (cm^2), $[O^{7+}/O] = 0.2$ and $[O/H] = 4.76 \times 10^{-6}$ are adopted after previous studies (Schwadron and Cravens 2000; Lepri et al. 2013) to simulate the solar wind conditions during the solar maximum period when soft X-ray missions will be launched.

In Figures 4a, b, we present X-ray intensity profiles P in the meridional plane at t = 160 s and t = 235 s, respectively. The envelope of the magnetopause is indicated by a dashed curve. In conjunction with Figures 2b, c, we find that if there is no HSJ impact on the magnetopause in the subsolar magnetosheath region (e.g., at t = 160 s), the magnetopause maintains a relatively smooth shape. When an HSJ is observed in the magnetosheath (e.g., at t = 235 s), there is an enhancement of X-ray intensity in the magnetosheath and a noticeable inward indentation of the magnetopause (indicated by arrows). Figure 4c is a similar plot to Figure 4b but estimated based on heavy ion O^{7+} data instead of proton data by Equation (3). Similarly, we can see significant deformation of the magnetopause, and the dynamical process and qualitative conclusions are almost the same as those estimated by solar wind protons. It implies that the estimation of X-ray intensity using solar wind proton data is a fine approximation in previous works. Bottom panels of Figure 4 show corresponding LOS integration values of I calculated by Equation (1) from a dawn-side view. The dashed and solid curves indicate the variation of the magnetopause location without (Figure 4a) and with (Figure 4b–c) indents caused by magnetosheath HSJs. Furthermore, a localized enhancement of LOS integrated intensity I is visible in the magnetosheath ahead of the magnetopause indents. It is expected to

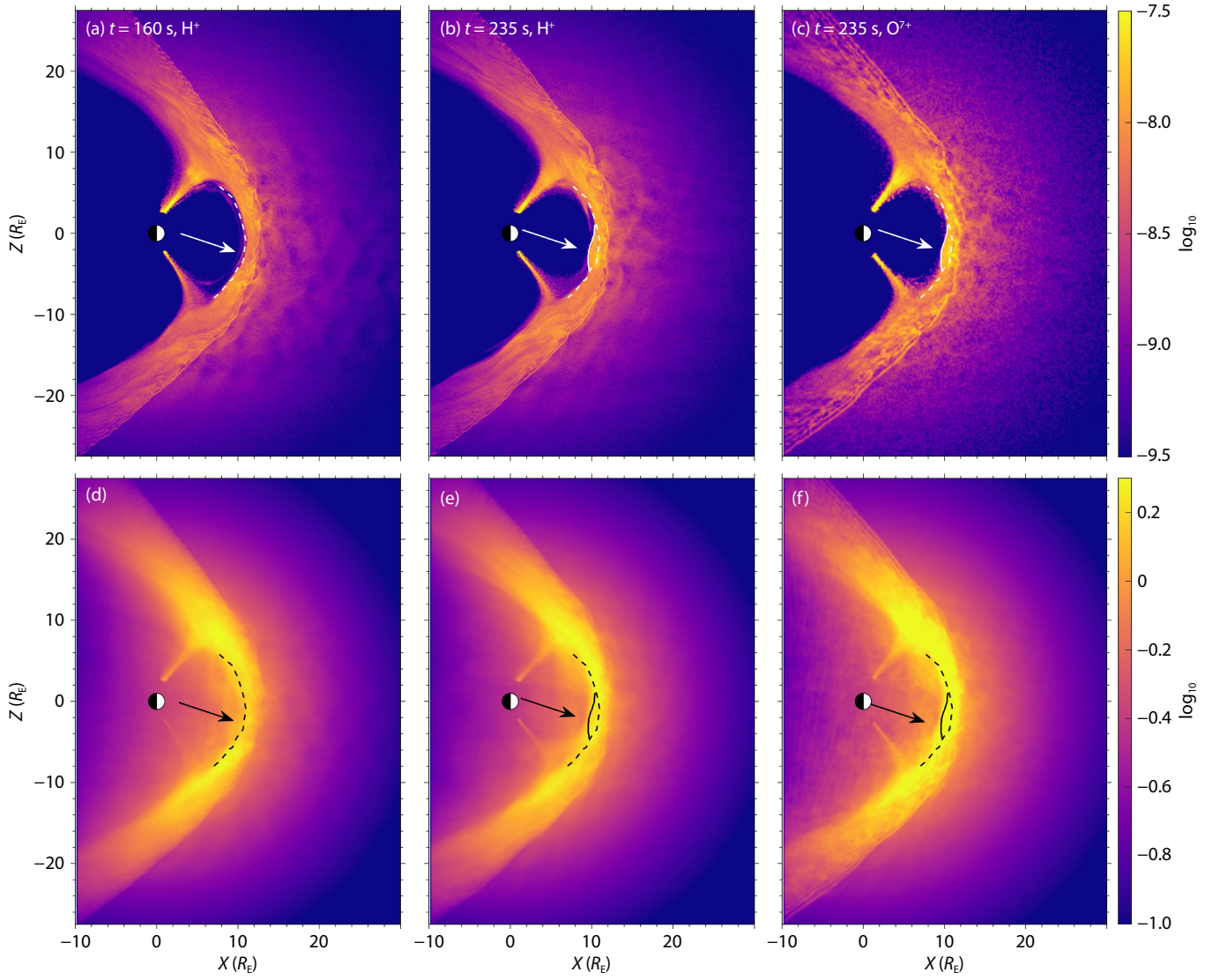

Figure 4. Top panels from left to right: (a–b) Snapshots of local X-ray intensity P in unit of (keV cm^{-3} s^{-1}) in the meridian plane calculated based on the solar wind H$^+$ data at t = 160 s and t = 235 s. (c) Similar plots to (b) but calculated based on the solar wind O^{7+} data. Bottom panels: (d–f) Corresponding Line-of-sight (LOS) integrated X-ray intensity I map in unit of (keV cm^{-2} s^{-1} sr^{-2}) calculated from a dawn-side view.

capture such localized brightening events by soft X-ray instruments from a dawnside-or duskside view on the Lunar orbit (e.g., NASA LEXI mission).

For a wide field-of-view, the Soft X-ray Imager (SXI) onboard SMILE uses lightweight micropore optics that provide high angular resolution (i.e., ~0.1°) for the 0.15–2.5 keV energy band (Branduardi–Raymont et al. 2018). To obtain good X-ray counts, SMILE/SXI is expected to achieve at least about 1.5° angular resolution near the dayside magnetopause (Connor et al. 2021). SXI has a field of view (FOV) of approximately 16° × 27°, and its line of sight forms a fixed angle with the UVI payload pointing towards the polar region and points towards the subsolar magnetopause. We have preliminarily calculated the profile of the LOS X-ray intensity integral value I within the FOV on SMILE's possible orbit, to study the possibility of SMILE imaging the deformation of the magnetopause caused by dynamic structures such as magnetosheath HSJs.

In Figure 5, the left panel shows a 3-D volume rendering sketch of the X-ray intensity. Key regions such as the cusp, magnetopause (MP), magnetosheath (MS), bow shock (BS), and the foreshock region are marked in the sketch. The field of view (FOV) of the SMILE spacecraft (SC) is also roughly denoted in yellow for reference. The motivation of this study is to find the best/potential location on the SMILE orbit for the imaging of magnetosheath transients (e.g., local dynamic pressure enhancements represented by HSJs) and magnetopause deformations. First, we use hybrid simulation to obtain 3-D intensity profiles at two fixed times (A: at 160 s and B: at 235 s); then, we calculate the LOS-integrated X-ray intensity I for these two fixed profiles observed by visual SC at different locations on the SMILE orbit. The selected locations of SC are shown in Figures 5c and f (an animation of this Figure is available for a full one-day orbit). When the spacecraft is located at [2.0, 8.6, 9.3] R_E (Figure 5c), the calculated LOS I images for the two fixed profiles A and B are shown in Figure 5a and b, respectively. The black rectangular area in Figure 5 encircles the field of view of SC in the θ and ϕ space. The black dashed curve describes the envelope from the cusp all the way to the magnetopause. By

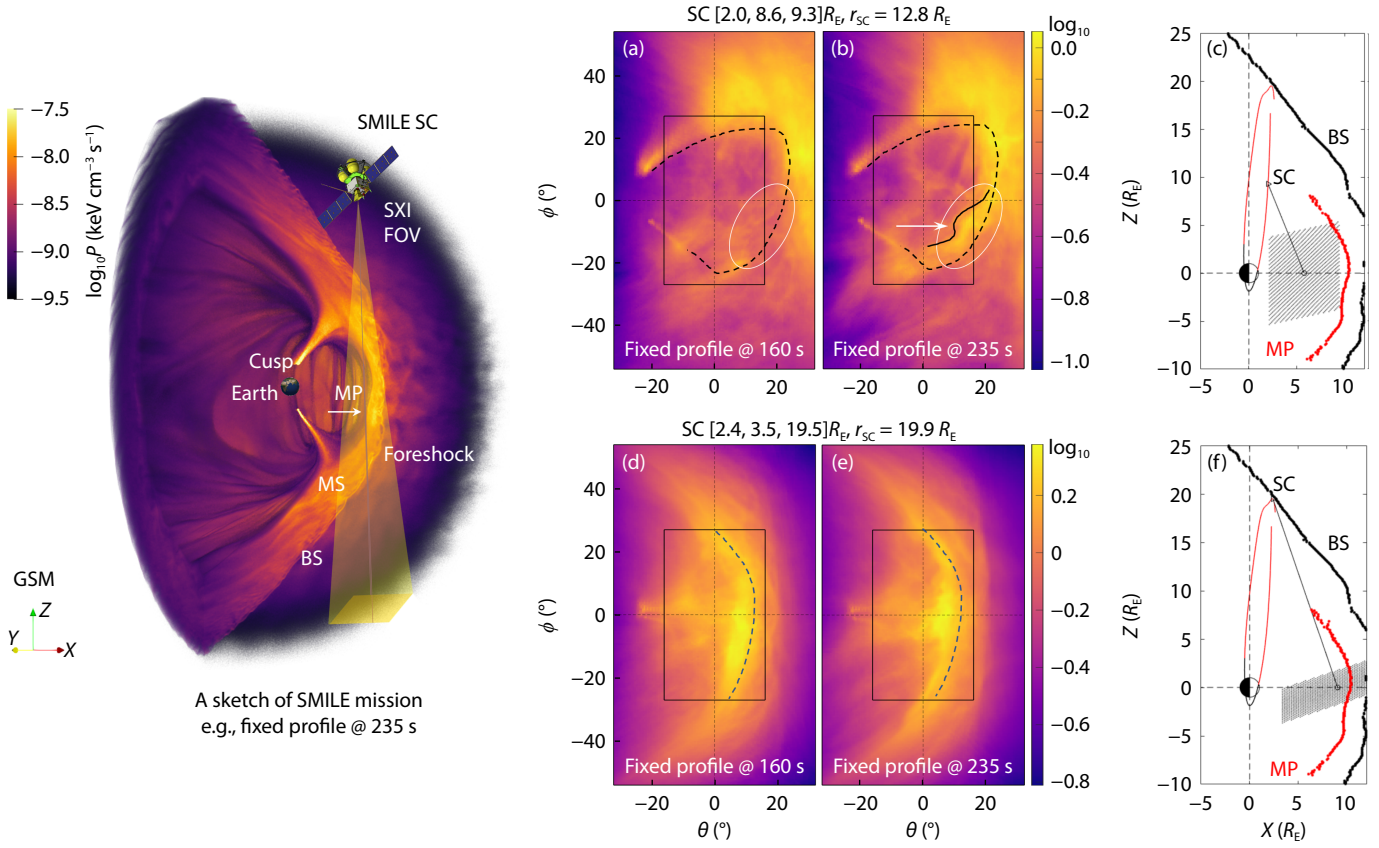

Figure 5. Left panel: A sketch of SMILE mission. Colors indicate a 3-D volume rendering of the X-ray intensity *P*. (a–b) At the same location [2.0, 8.6, 9.3] R_E on the polar orbit, LOS integrated *I* calculated for different *P* profiles issued from the simulation at t = 160 s and t = 235 s are represented for comparison. (c) Corresponding spacecraft (SC), magnetopause (MP), and bow shock (BS) locations relative to the Earth and its FOV are shown for reference. (d–f) Similar plots as (a–c) but for another SC location [2.4, 3.5, 19.5] R_E at higher latitude on the polar orbit.

comparing the region where HSJs impact the magnetopause (the area marked by white circles), it is clearly evidenced that the shape of the magnetopause impacted by HSJs has undergone significant indentation and is accompanied by local X-ray brightening. This conclusion is very interesting and can at least indicate that under the current height and spacecraft attitude orientation conditions shown in Figure 5c, it is very likely to capture the magnetosheath solar wind-magnetopause coupling process. Furthermore, in Figures 5d and e, we also calculated the LOS X-ray for imaging the magnetopause from a bird's-eye view under spacecraft apogee conditions on orbit. At the apogee, it is good for the SC to capture the entire geometry of the magnetopause, but LOS-integration effects may make it difficult to identify magnetosheath HSJs or local concavity and convexity of magnetopause in a smaller dynamic or kinetic scales. In summary, it means that at different locations on the SC orbit, there are advantages and disadvantages in imaging dynamic structures, magnetopause deformation, and overall geometries of the whole magnetopause.

4. Conclusions and Discussions

This article mainly uses 3D global hybrid simulation to study the dynamics of the Earth's bow shock and magnetosphere under radial IMF conditions and conducts soft X-ray imaging tests. The main conclusions are:

(1) Under radial solar wind conditions, the subsolar magnetosheath falls downstream of the quasi-parallel shock. Here, a large number of HSJs have been observed, which is consistent with previous Cluster and MMS statistical observations (e.g., Escoubet et al. 2020) In addition, HSJs have a good correspondence with ULF steepening transients of the foreshock.

(2) The simulation in this article not only reproduces that the spatial size of HSJs can reach the order of magnitude of the Earth's radius, which is consistent with previous global simulations (e.g., Chen LJ et al. 2021). Moreover, it is also found that HSJs can last for seconds to minutes at the subsolar point and impact the magnetopause to form a depression.

(3) We analyzed the discrimination ability of different spacecraft positions on local deformation of the magnetopause at an approximate lunar orbit of 60 R_E and SMILE's possible orbit. The main conclusion is that the LOS X-ray imaging observed on the lunar orbit (such as LEXI) has a good ability to identify the magnetopause deformation within the meridian plane; polar orbit spacecrafts (such as SMILE) have advantages in imaging the overall geometry of the magnetopause within the equatorial plane at its apogee. One striking point is that SMILE may have the potential ability to capture small-scale transient structures (e.g., HSJs) at low altitudes around the magnetopause.

In the near future, we need to consider the background noise,

different IMF conditions, the asymmetric exosphere neutral hydrogen profile, and solar wind structures, e.g., CME, TD, RD, CS (Modolo et al. 2012; Guo ZF et al. 2021) on the soft X-ray imaging. The main goal is to provide pre-studies as much as we can to serve the data analysis for the future soft X-ray space missions around 2025 during the solar maximum.

Acknowledgments

Authors are grateful to Daniel Weimer from Virginia Tech, Urs Ganse and Yann Kempf from University of Helsinki, San Lu from USTC, and Chuanfei Dong from Boston University for helpful discussions. This work was supported by the National Key R&D program of China No.2021YFA0718600, NNFSC grants 42150105, 42188101, and 42274210, and the Specialized Research Fund for State Key Laboratories of China. The computations are performed by Numerical Forecast Modeling R&D and VR System of State Key Laboratory of Space Weather, and HPC of Chinese Meridian Project using the RHybrid code distributed under the open source GPL v3 license by the Finnish Meteorological Institute (github.com/fmihpc/rhybrid).

References

Bessho, N., Chen, L.-J., Stawarz, J. E., Wang, S., Hesse, M., Wilson , L. B., and Ng, J. (2022). Strong reconnection electric fields in shock-driven turbulence. *Phys. Plasmas*, *29*(4), 042304. https://doi.org/10.1063/5.0077529

Blanco-Cano, X., Omidi, N., and Russell, C. T. (2006). Macrostructure of collisionless bow shocks: 2. ULF waves in the foreshock and magnetosheath. *J. Geophys. Res.: Space Phys.*, *111*(A10), A10205. https://doi.org/10.1029/2005JA011421

Branduardi-Raymont, G., Elsner, R. F., Gladstone, G. R., Ramsay, G., Rodriguez, P., Soria, R., and Waite, Jr. J. H. (2004). First observation of Jupiter by XMM-Newton. *Astron. Astrophys.*, *424*(1), 331–337. https://doi.org/10.1051/0004-6361:20041149

Branduardi-Raymont, G., Sembay, S., Carter, J., and Ezoe, Y. (2018). Exploring geospace via solar wind charge exchange X-rays. In *European Planetary Science Congress 2018*. Berlin: TU Berlin.

Burch, J. L., Torbert, R. B., Phan, T. D., Chen, L.-J., Moore, T. E., Ergun, R. E., Eastwood, J. P., Gershman, D. J., Cassak, P. A., … Chandler, M. (2016). Electron-scale measurements of magnetic reconnection in space. *Science*, *352*(6290), 2939. https://doi.org/10.1126/science.aaf2939

Burgess, D., Wilkinson, W. P., and Schwartz, S. J. (1989). Ion distributions and thermalization at perpendicular and quasi-perpendicular supercritical collisionless shocks. *J. Geophys. Res.: Space Phys.*, *94*(A7), 8783. https://doi.org/10.1029/JA094iA07p08783

Burgess, D., Lucek, E. A., Scholer, M., Bale, S. D., Balikhin, M. A., Balogh, A., Horbury, T. S., Krasnoselskikh, V. V., Kucharek, H., … Walker, S. N. (2005). Quasi-parallel shock structure and processes. *Space Sci. Rev.*, *118*(1-4), 205–222. https://doi.org/10.1007/s11214-005-3832-3

Burgess, D., and Scholer, M. (2013). Microphysics of quasi-parallel shocks in collisionless plasmas. *Space Sci. Rev.*, *178*(2), 513–533. https://doi.org/10.1007/s11214-013-9969-6

Chen, L. J., Ng, J., Omelchenko, Y., and Wang, S. (2021). Magnetopause reconnection and indents induced by foreshock turbulence. *Geophys. Res. Lett.*, *48*(11), e2021GL093029. https://doi.org/10.1029/2021GL093029

Collier, M. R., Snowden, S. L., Sarantos, M., Benna, M., Carter, J. A., Cravens, T. E., Farrell, W. M., Fatemi, S., Kent Hills, H., … Walsh, B. M. (2014). On lunar exospheric column densities and solar wind access beyond the terminator from ROSAT soft X-ray observations of solar wind charge exchange. *J. Geophys. Res.: Planets*, *119*(7), 1459–1478. https://doi.org/10.1002/2014JE004628

Connor, H. K., Sibeck, D. G., Collier, M. R., Baliukin, I. I., Branduardi-Raymont, G., Brandt, P. C., Buzulukova, N. Y., Collado-Vega, Y. M., Escoubet, C. P., … Zoennchen, J. H. (2021). Soft X-ray and ENA imaging of the Earth's dayside magnetosphere. *J. Geophys. Res.: Space Phys.*, *126*(3), e2020JA028816. https://doi.org/10.1029/2020JA028816

Cravens, T. E. (1997). Comet Hyakutake X-ray source: charge transfer of solar wind heavy ions. *Geophys. Res. Lett.*, *24*(1), 105–108. https://doi.org/10.1029/96GL03780

Cravens, T. E. (2000). Heliospheric X-ray emission associated with charge transfer of the solar wind with interstellar neutrals. *Astrophys. J.*, *532*(2), L153–L156. https://doi.org/10.1086/312574

Cravens, T. E., Robertson, I. P., and Snowden, S. L. (2001). Temporal variations of geocoronal and heliospheric X-ray emission associated with the solar wind interaction with neutrals. *J. Geophys. Res.: Space Phys.*, *106*(A11), 24883–24892. https://doi.org/10.1029/2000JA000461

Dennerl, K., Lisse, C. M., Bhardwaj, A., Burwitz, V., Englhauser, J., Gunell, H., Holmström, M., Jansen, F., Kharchenko, V., and Rodríguez-Pascual, P. M. (2006). First observation of Mars with XMM-Newton: high resolution X-ray spectroscopy with RGS. *Astron. Astrophys.*, *451*(2), 709–722. https://doi.org/10.1051/0004-6361:20054253

Escoubet, C. P., Hwang, K. J., Toledo-Redondo, S., Turc, L., Haaland, S. E., Aunai, N., Dargent, J., Eastwood, J. P., Fear, R. C., … Torbert, R. B. (2020). Cluster and MMS simultaneous observations of magnetosheath high speed jets and their impact on the magnetopause. *Front. Astron. Space Sci.*, *6*, 78. https://doi.org/10.3389/fspas.2019.00078

Farrugia, C. J., Gratton, F. T., Gnavi, G., Torbert, R. B., and Wilson, L. B. (2014). A vortical dawn flank boundary layer for near-radial IMF: Wind observations on 24 October 2001. *J. Geophys. Res.: Space Phys.*, *119*(6), 4572–4590. https://doi.org/10.1002/2013JA019578

Fatemi, S., Poirier, N., Holmström, M., Lindkvist, J., Wieser, M., and Barabash, S. (2018). A modelling approach to infer the solar wind dynamic pressure from magnetic field observations inside Mercury's magnetosphere. *Astron. Astrophys.*, *614*, A132. https://doi.org/10.1051/0004-6361/201832764

Fatemi, S., Poppe, A. R., and Barabash, S. (2020). Hybrid simulations of solar wind proton precipitation to the surface of mercury. *J. Geophys. Res.: Space Phys.*, *125*(4), e2019JA027706. https://doi.org/10.1029/2019JA027706

Fujimoto, R., Mitsuda, K., McCammon, D., Takei, Y., Bauer, M., Ishisaki, Y., Scott Porter, F., Yamaguchi, H., Hayashida, K., and Yamasaki, N. Y. (2007). Evidence for solar-wind charge-exchange X-ray emission from the Earth's magnetosheath. *Progr. Theor. Phys. Suppl.*, *169*, 71–74. https://doi.org/10.1143/PTPS.169.71

Gingell, I., Schwartz, S. J., Eastwood, J. P., Stawarz, J. E., Burch, J. L., Ergun, R. E., Fuselier, S. A., Gershman, D. J., Giles, B. L., …Wilder, F. (2020). Statistics of reconnecting current sheets in the transition region of Earth's bow shock. *J. Geophys. Res.: Space Phys.*, *125*(1), e2019JA027119. https://doi.org/10.1029/2019JA027119

Grandin, M., Connor, H. K., Hoilijoki, S., Battarbee, M., Pfau-Kempf, Y., Ganse, U., Papadakis, K., and Palmroth, M. (2024). Hybrid-Vlasov simulation of soft X-ray emissions at the Earth's dayside magnetospheric boundaries. *Earth Planet. Phys.*, *8*(1), 70–88. https://doi.org/10.26464/epp2023052

Gunell, H., Kallio, E., Jarvinen, R., Janhunen, P., Holmström, M., and Dennerl, K. (2007). Simulations of solar wind charge exchange X-ray emissions at Venus. *Geophys. Res. Lett.*, *34*(3), L03107. https://doi.org/10.1029/2006GL028602

Guo, J., Lu, S., Lu, Q. M., Lin, Y., Wang, X. Y., Ren, J. Y., Hao, Y. F., Huang, K., Wang, R. S., and Gao, X. L. (2022). Large-scale high-speed jets in Earth's magnetosheath: global hybrid simulations. *J. Geophys. Res.: Space Phys.*, *127*(6), e30477. https://doi.org/10.1029/2022JA030477

Guo, X. C., Wang, C., and Hu, Y. Q. (2010). Global MHD simulation of the Kelvin-Helmholtz instability at the magnetopause for northward interplanetary magnetic field. *J. Geophys. Res.: Space Phys.*, *115*(A10), A10218. https://doi.org/10.1029/2009JA015193

Guo, Z. F., Lin, Y., and Wang, X. Y. (2021). Investigation of the interaction between magnetosheath reconnection and magnetopause reconnection driven by oblique interplanetary tangential discontinuity using three-dimensional global hybrid simulation. *J. Geophys. Res.: Space Phys.*, *126*(2), e28558. https://doi.org/10.1029/2020JA028558

Han, D. S., Hietala, H., Chen, X. C., Nishimura, Y., Lyons, L. R., Liu, J. J., Hu, H. Q., and Yang, H. G. (2017). Observational properties of dayside throat aurora

and implications on the possible generation mechanisms. *J. Geophys. Res.*: *Space Phys.*, *122*(2), 1853–1870. https://doi.org/10.1002/2016JA023394

Hao, Y., Lembege, B., Lu, Q., and Guo, F. (2016). Formation of downstream high-speed jets by a rippled nonstationary quasi-parallel shock: 2-D hybrid simulations. *J. Geophys. Res.*: *Space Phys.*, *121*(3), 2080–2094. https://doi.org/10.1002/2015JA021419

Hao, Y. F., Gao, X. L., Lu, Q. M., Huang, C., Wang, R. S., and Wang, S. (2017). Reformation of rippled quasi-parallel shocks: 2-D hybrid simulations. *J. Geophys. Res.*: *Space Phys.*, *122*(6), 6385–6396. https://doi.org/10.1002/2017JA024234

Hietala, H., and Plaschke, F. (2013). On the generation of magnetosheath high–speed jets by bow shock ripples. *J. Geophys. Res.*: *Space Phys.*, *118*(11), 7237–7245. https://doi.org/10.1002/2013JA019172

Hietala, H., Laitinen, T. V., Andréeová, K., Vainio, R., Vaivads, A., Palmroth, M., Pulkkinen, T. I., Koskinen, H. E. J., Lucek, E. A., and Rème, H. (2009). Supermagnetosonic jets behind a collisionless quasiparallel shock. *Phys. Rev. Lett.*, *103*(24), 245001. https://doi.org/10.1103/PhysRevLett.103.245001

Holmström, M., Barabash, S., and Kallio, E. (2001). X-ray imaging of the solar wind—Mars interaction. *Geophys. Res. Lett.*, *28*(7), 1287–1290. https://doi.org/10.1029/2000GL012381

Hu, Y. Q., Guo, X. C., and Wang, C. (2007). On the ionospheric and reconnection potentials of the Earth: results from global MHD simulations. *J. Geophys. Res.*: *Space Phys.*, *112*(A7), A07215. https://doi.org/10.1029/2006JA012145

Huang, S. Y., Wei, Y. Y., Zhao, J. S., Yuan, Z. G., Deng, X. H., Jiang, K., Xu, S. B., Zhang, J., Xiong, Q. Y.,... Lin, R. T. (2022). Kinetic-size magnetic holes in the terrestrial foreshock region. *Geophys. Res. Lett.*, *49*(8), e2021GL093813. https://doi.org/10.1029/2021GL093813

Jarvinen, R., Brain, D. A., Modolo, R., Fedorov, A., and Holmström, M. (2018). Oxygen ion energization at Mars: comparison of MAVEN and Mars express observations to global hybrid simulation. *J. Geophys. Res.*: *Space Phys.*, *123*(2), 1678–1689. https://doi.org/10.1002/2017JA024884

Jarvinen, R., Alho, M., Kallio, E., and Pulkkinen, T. I. (2020). Ultra-low-frequency waves in the ion foreshock of Mercury: a global hybrid modelling study. *Mon. Not. Roy. Astron. Soc.*, *491*(3), 4147–4161. https://doi.org/10.1093/mnras/stz3257

Jarvinen, R., Kallio, E., and Pulkkinen, T. I. (2022). Ultra-low frequency foreshock waves and ion dynamics at Mars. *J. Geophys. Res.*: *Space Phys.*, *127*(5), e2021JA030078. https://doi.org/10.1029/2021JA030078

Jiang, K., Huang, S. Y., Fu, H. S., Yuan, Z. G., Deng, X. H., Wang, Z., Guo, Z. Z., Xu, S. B., Wei, Y. Y., … Yu, L. (2021). Observational evidence of magnetic reconnection in the terrestrial foreshock region. *Astrophys. J.*, *922*(1), 56. https://doi.org/10.3847/1538-4357/ac2500

Johlander, A., Schwartz, S. J., Vaivads, A., Khotyaintsev, Y. V., Gingell, I., Peng, I. B., Markidis, S., Lindqvist, P. A., Ergun, R. E., … Burch, J. L. (2016). Rippled quasiperpendicular shock observed by the magnetospheric multiscale spacecraft. *Phys. Rev. Lett.*, *117*(16), 165101. https://doi.org/10.1103/PhysRevLett.117.165101

Jorgensen, A. M., Sun, T. R., Wang, C., Dai, L., Sembay, S., Wei, F., Guo, Y. H., and Xu, R. L. (2019). Boundary detection in three dimensions with application to the SMILE mission: the effect of photon noise. *J. Geophys. Res.*: *Space Phys.*, *124*(6), 4365–4383. https://doi.org/10.1029/2018JA025919

Kallio, E., Jarvinen, R., Massetti, S., Alberti, T., Milillo, A., Orsini, S., De Angelis, E., Laky, G., Slavin, J., … Pulkkinen, T. I. (2022). Ultra-low frequency waves in the hermean magnetosphere: on the role of the morphology of the magnetic field and the foreshock. *Geophys. Res. Lett.*, *49*(24), e2022GL101850. https://doi.org/10.1029/2022GL101850

Karimabadi, H., Roytershteyn, V., Vu, H. X., Omelchenko, Y. A., Scudder, J., Daughton, W., Dimmock, A., Nykyri, K., Wan, M., … Geveci, B. (2014). The link between shocks, turbulence, and magnetic reconnection in collisionless plasmas. *Phys. Plasmas*, *21*(6), 062308. https://doi.org/10.1063/1.4882875

Koutroumpa, D., Lallement, R., Kharchenko, V., Dalgarno, A., Pepino, R., Izmodenov, V., and Quémerais, E. (2006). Charge-transfer induced EUV and soft X-ray emissions in the heliosphere. *Astron. Astrophys.*, *460*(1), 289–300. https://doi.org/10.1051/0004-6361:20065250

Koutroumpa, D., Modolo, R., Chanteur, G., Chaufray, J. Y., Kharchenko, V., and Lallement, R. (2012). Solar wind charge exchange X-ray emission from Mars: model and data comparison. *Astron. Astrophys.*, *545*, A153. https://doi.org/10.1051/0004-6361/201219720

Larrodera, C., and Cid, C. (2020). Bimodal distribution of the solar wind at 1 AU. *Astron. Astrophys.*, *635*, A44. https://doi.org/10.1051/0004-6361/201937307

Lembege, B., and Savoini, P. (1992). Nonstationarity of a two-dimensional quasiperpendicular supercritical collisionless shock by self-reformation. *Phys. Fluids B*: *Plasma Phys.*, *4*(11), 3533–3548. https://doi.org/10.1063/1.860361

Lembege, B., Giacalone, J., Scholer, M., Hada, T., Hoshino, M., Krasnoselskikh, V., Kucharek, H., Savoini, P., and Terasawa. T. (2004). Selected problems in collisionless-shock physics. *Space Sci. Rev.*, *110*(3-4), 161–226. https://doi.org/10.1023/B:SPAC.0000023372.12232.b7

Lepri, S. T., Landi, E., and Zurbuchen, T. H. (2013). Solar wind heavy ions over solar cycle 23: ACE/SWICS measurements. *Astrophys. J.*, *768*(1), 94. https://doi.org/10.1088/0004-637X/768/1/94

Li, W. Y., Guo, X. C., and Wang, C. (2012). Spatial distribution of Kelvin-Helmholtz instability at low-latitude boundary layer under different solar wind speed conditions. *J. Geophys. Res.*: *Space Phys.*, *117*(A8), A08230. https://doi.org/10.1029/2012JA017780

Lin, Y., Wang, X. Y., Lu, S., Perez, J. D., and Lu, Q. (2014). Investigation of storm time magnetotail and ion injection using three-dimensional global hybrid simulation. *J. Geophys. Res.*: *Space Phys.*, *119*(9), 7413–7432. https://doi.org/10.1002/2014JA020005

Lisse, C. M., Dennerl, K., Englhauser, J., Harden, M., Marshall, F. E., Mumma, M. J., Petre, R., Pye, J. P., Ricketts, M. J., … West, R. G. (1996). Discovery of X-ray and extreme ultraviolet emission from comet C/Hyakutake 1996 B2. *Science*, *274*(5285), 205–209. https://doi.org/10.1126/science.274.5285.205

Liu, M. Z., Yang, Z. W., Liu, Y. D., Lembége, B., Issautier, K., Wilson , L. B., Zhao, S. Q., Jagarlamudi, V. K., Zhao, X. W., … Chrysaphi, N. (2022). Properties of a supercritical quasi-perpendicular interplanetary shock propagating in the terrestrial foreshock region. *Astrophys. J. Suppl. Ser.*, *263*(1), 11. https://doi.org/10.3847/1538-4365/ac94c8

Liu, T. Z., Hao, Y. F., Wilson, L. B., Turner, D. L., and Zhang, H. (2021). Magnetospheric multiscale observations of Earth's oblique bow shock reformation by foreshock ultralow-frequency waves. *Geophys. Res. Lett.*, *48*(2), e91184. https://doi.org/10.1029/2020GL091184

Lu, Q. M., Yang, Z. W., Wang, H. Y., Wang, R. S., Huang, K., Lu, S., and Wang, S. (2021). Two-dimensional particle-in-cell simulation of magnetic reconnection in the downstream of a quasi-perpendicular shock. *Astrophys. J.*, *919*(1), 28. https://doi.org/10.3847/1538-4357/ac18c0

Matsukiyo, S., and Scholer, M. (2003). Modified two-stream instability in the foot of high Mach number quasi-perpendicular shocks. *J. Geophys. Res.*: *Space Phys.*, *108*(A12), 1459. https://doi.org/10.1029/2003JA010080

Matsumoto, Y., and Miyoshi, Y. (2022). Soft X-ray imaging of magnetopause reconnection outflows under low plasma-β solar wind conditions. *Geophys. Res. Lett.*, *49*(19), e2022GL101037. https://doi.org/10.1029/2022GL101037

Modolo, R., Chanteur, G. M., and Dubinin, E. (2012). Dynamic Martian magnetosphere: transient twist induced by a rotation of the IMF. *Geophys. Res. Lett.*, *39*(1), L01106. https://doi.org/10.1029/2011GL049895

Nakamura, T. K. M., Hasegawa, H., Daughton, W., Eriksson, S., Li, W. Y., and Nakamura, R. (2017). Turbulent mass transfer caused by vortex induced reconnection in collisionless magnetospheric plasmas. *Nat. Commun.*, *8*, 1582. https://doi.org/10.1038/s41467-017-01579-0

Ng, J., Chen, L. J., and Omelchenko, Y. A. (2021). Bursty magnetic reconnection at the Earth's magnetopause triggered by high-speed jets. *Phys. Plasmas*, *28*(9), 092902. https://doi.org/10.1063/5.0054394

Omelchenko, Y. A., Chen, L. J., and Ng, J. (2021). 3D space-time adaptive hybrid simulations of magnetosheath high-speed jets. *J. Geophys. Res.*: *Space Phys.*, *126*(7), e2020JA029035. https://doi.org/10.1029/2020JA029035

Otsuka, F., Matsukiyo, S., and Hada, T. (2019). PIC simulation of a quasi-parallel collisionless shock: interaction between upstream waves and backstreaming ions. *High Energy Dens. Phys.*, *33*, 100709. https://doi.org/10.1016/j.hedp.2019.100709

Palmroth, M., Archer, M., Vainio, R., Hietala, H., Pfau-Kempf, Y., Hoilijoki, S., Hannuksela, O., Ganse, U., Sandroos, A., … Eastwood, J. P. (2015). ULF foreshock under radial IMF: THEMIS observations and global kinetic simulation Vlasiator results compared. *J. Geophys. Res.*: *Space Phys.*, *120*(10), 8782–8798. https://doi.org/10.1002/2015JA021526

Palmroth, M., Raptis, S., Suni, J., Karlsson, T., Turc, L., Johlander, A., Ganse, U., Pfau-Kempf, Y., Blanco-Cano, X., … Osmane, A. (2021). Magnetosheath jet evolution as a function of lifetime: global hybrid-Vlasov simulations compared to MMS observations. *Ann. Geophys.*, *39*(2), 289–308. https://doi.org/10.5194/angeo-39-289-2021

Pepino, R., Kharchenko, V., Dalgarno, A., and Lallement, R. (2004). Spectra of the X-ray emission induced in the interaction between the solar wind and the heliospheric gas. *Astrophys. J.*, *617*(2), 1347–1352. https://doi.org/10.1086/425682

Phan, T. D., Eastwood, J. P., Shay, M. A., Drake, J. F., Sonnerup, B. U. Ö., Fujimoto, M., Cassak, P. A., Øieroset, M., Burch, J. L., … Magnes, W. (2018). Electron magnetic reconnection without ion coupling in Earth's turbulent magnetosheath. *Nature*, *557*(7704), 202–206. https://doi.org/10.1038/s41586-018-0091-5

Pi, G., Pitňa, A., Zhao, G. Q., Němeček, Z., Šafránková, J., and Tsai, T. C. (2022). Properties of magnetic field fluctuations in long-lasting radial IMF events from wind observation. *Atmosphere*, *13*(2), 173. https://doi.org/10.3390/atmos13020173

Plaschke, F., Hietala, H., Archer, M., Blanco-Cano, X., Kajdič, P., Karlsson, T., Lee, S. H., Omidi, N., Palmroth, M., … Sibeck, D. (2018). Jets downstream of collisionless shocks. *Space Sci. Rev.*, *214*(5), 81. https://doi.org/10.1007/s11214-018-0516-3

Preisser, L., Blanco-Cano, X., Kajdič, P., Burgess, D., and Trotta, D. (2020). Magnetosheath jets and plasmoids: characteristics and formation mechanisms from hybrid simulations. *Astrophys. J. Lett.*, *900*(1), L6. https://doi.org/10.3847/2041-8213/abad2b

Raeder, J. (2003). Global magnetohydrodynamics—a tutorial. In J. Büchner, et al. (Eds.), *Space Plasma Simulation*. Berlin: Springer. https://doi.org/10.1007/3-540-36530-3_11

Raptis, S., Karlsson, T., Vaivads, A., Pollock, C., Plaschke, F., Johlander, A., Trollvik, H., and Lindqvist, P. A. (2022). Downstream high-speed plasma jet generation as a direct consequence of shock reformation. *Nat. Commun.*, *13*(1), 598. https://doi.org/10.1038/s41467-022-28110-4

Robertson, I. P., and Cravens, T. E. (2003). X-ray emission from the terrestrial magnetosheath. *Geophys. Res. Lett.*, *30*(8), 1439. https://doi.org/10.1029/2002GL016740

Scholer, M., Shinohara, I., and Matsukiyo, S. (2003). Quasi-perpendicular shocks: length scale of the cross-shock potential, shock reformation, and implication for shock surfing. *J. Geophys. Res.*: *Space Phys.*, *108*(A1), SSH 4-1–SSH 4-11. https://doi.org/10.1029/2002JA009515

Schwadron, N. A., and Cravens, T. E. (2000). Implications of solar wind composition for cometary X-rays. *Astrophys. J.*, *544*(1), 558–566. https://doi.org/10.1086/317176

Schwartz, S. J., and Burgess, D. (1991). Quasi-parallel shocks: a patchwork of three-dimensional structures. *Geophys. Res. Lett.*, *18*(3), 373–376. https://doi.org/10.1029/91GL00138

Sibeck, D. G., Allen, R., Aryan, H., Bodewits, D., Brandt, P., Branduardi-Raymont, G., Brown, G., Carter, J. A., Collado-Vega, Y. M., … Wing, S. (2018). Imaging plasma density structures in the soft X-rays generated by solar wind charge exchange with neutrals. *Space Sci. Rev.*, *214*(4), 79. https://doi.org/10.1007/s11214-018-0504-7

Sun, T. R., Wang, C., Wei, F., and Sembay, S. (2015). X-ray imaging of Kelvin-Helmholtz waves at the magnetopause. *J. Geophys. Res.*: *Space Phys.*, *120*(1), 266–275. https://doi.org/10.1002/2014JA020497

Sun, T. R., Wang, C., Sembay, S. F., Lopez, R. E., Escoubet, C. P., Branduardi-Raymont, G., Zheng, J. H., Yu, X. Z., Guo, X. C., … Guo, Y. H. (2019). Soft X-ray imaging of the magnetosheath and cusps under different solar wind conditions: MHD simulations. *J. Geophys. Res.*: *Space Phys.*, *124*(4), 2435–2450. https://doi.org/10.1029/2018JA026093

Tinoco-Arenas, A., Kajdič, P., Preisser, L., Blanco-Cano, X., Trotta, D., and Burgess, D. (2022). Parametric study of magnetosheath jets in 2D local hybrid simulations. *Front. Astron. Space Sci.*, *9*, 5. https://doi.org/10.3389/fspas.2022.793195

Wang, S., Chen, L. J., Ng, J., Bessho, N., Le, G., Fung, S. F., Gershman, D. J., and Giles, B. L. (2021). A statistical study of three-second foreshock ULF waves observed by the Magnetospheric Multiscale mission. *Phys. Plasmas*, *28*(8), 082901. https://doi.org/10.1063/5.0055972

Wargelin, B. J., Markevitch, M., Juda, M., Kharchenko, V., Edgar, R., and Dalgarno, A. (2004). *Chandra* observations of the "dark" moon and geocoronal solar wind charge transfer. *Astrophys. J.*, *607*(1), 596–610. https://doi.org/10.1086/383410

Watari, S., Vandas, M., and Watanabe, T. (2005). Solar cycle variation of long-duration radial interplanetary magnetic field events at 1 AU. *J. Geophys. Res.*: *Space Phys.*, *110*(A12), A12102. https://doi.org/10.1029/2005JA011165

Wegmann, R., and Dennerl, K. (2005). X-ray tomography of a cometary bow shock. *Astron. Astrophys.*, *430*(2), L33–L36. https://doi.org/10.1051/0004-6361:200400124

Wilson, L. B., Koval, A., Sibeck, D. G., Szabo, A., Cattell, C. A., Kasper, J. C., Maruca, B. A., Pulupa, M., Salem, C. S., and Wilber, M. (2013). Shocklets, SLAMS, and field-aligned ion beams in the terrestrial foreshock. *J. Geophys. Res.*: *Space Phys.*, *118*(3), 957–966. https://doi.org/10.1029/2012JA018186

Winske, D., and Quest, K. B. (1988). Magnetic field and density fluctuations at perpendicular supercritical collisionless shocks. *J. Geophys. Res.*: *Space Phys.*, *93*(A9), 9681–9693. https://doi.org/10.1029/JA093iA09p09681

Yang, Z. W., Liu, Y. D., Matsukiyo, S., Lu, Q. M., Guo, F., Liu, M. Z., Xie, H. S., Gao, X. L., and Guo, J. (2020). PIC simulations of microinstabilities and waves at near-sun solar wind perpendicular shocks: predictions for Parker Solar Probe and Solar Orbiter. *Astrophys. J. Lett.*, *900*(2), L24. https://doi.org/10.3847/2041-8213/abaf59

Zhang, Y. J., Sun, T. R., Wang, C., Ji, L., Carter, J. A., Sembay, S., Koutroumpa, D., Liu, Y. D., Liang, G. Y., … Zhao, X. W. (2022). Solar wind charge exchange soft x-ray emissions in the magnetosphere during an interplanetary coronal mass ejection compared to its driven sheath. *Astrophys. J. Lett.*, *932*(1), L1. https://doi.org/10.3847/2041-8213/ac7521